B. Re, C. Dobrzynski, A. Guardone
Assessment of Grid Adaptation Criteria for Steady, Two-Dimensional, Inviscid Flows in Non-Ideal Compressible Fluids
Applied Mathematics and Computation, Vol. 319, 2018, p. 337-354
doi:10.1016/j.amc.2017.03.049

Assessment of grid adaptation criteria for steady, two-dimensional, inviscid flows in non-ideal compressible fluids

B. Re[a,*], C. Dobrzynski[b], A. Guardone[a]

[a] *Department of Aerospace Science and Technology, Politecnico di Milano, via La Masa 34, 20156 Milano, Italy*
[b] *Bordeaux-INP/Inria Bordeaux — Sud-Ouest, 200 avenue de la Vieille Tour, 33405 Talence cedex*

Abstract

Two-dimensional simulations are carried out to assess standard grid adaptation criteria, widely used for ideal flows, for steady inviscid flows in the proximity of the liquid-vapor saturation curve, where non-ideal compressible-fluid behavior is expected. A van der Waals fluid description of the thermodynamic properties is assumed to account for non-ideal effects at least qualitatively. Nitrogen under-expanded nozzle jets are chosen as the reference flow to assess different adaptation criteria. Isotropic and anisotropic error estimators based on the derivatives of flow variables proved to be suitable to capture the rarefaction, the reflected shock and the constant-pressure jet boundary. Both density and Mach-based estimators are found to be very suitable to drive grid adaptation in the non-ideal compressible-fluid regime, which is characterized by large fluid compressibility. Then, similar adaptation criteria were used to simulate under-expanded nozzle jets of the siloxane MDM, an high molecular complexity fluid for which the van der Waals model predicts the existence of a thermodynamic region where the fundamental derivative of gasdynamics has values less than one. In this region, Mach number estimators proved to be more effective because of the non-ideal dependence of the speed of sound on the density and the temperature.

Keywords: Non-Ideal Compressible-Fluid Dynamics (NICFD), Unstructured mesh adaptation, Van der Waals fluids, Finite volume scheme, Under-expanded jets

1. Introduction

Mesh adaptation proved to be a valuable tool for numerical simulations of fluid flows [1], with particular reference to fluid flows characterized by different spatial scales and to all situations where the general location of relevant flow features is not known a priori [2, 3, 4]. As it is well known, adaptation techniques aim at modifying the computational mesh to maximize its efficiency with respect to a given goal, therefore the definition of the criterion used to modify grid spacing is a key point in mesh adaptation [5] and several approaches have been proposed. For example, integral error indicators obtained from the solution of the adjoint flow problem can be used to redistribute the mesh nodes to minimize the error in the evaluation of the output of interest, such as the aerodynamic force acting on a given solid body [6, 7, 8]. However, if not already available for some other purposes, the solution of the adjoint problem may be expensive [9]. Alternatively, a suitable local error indicator can be built and the grid can be modified to equi-distribute the numerical error within the computational domain, i.e. the local mesh size can be increased (decreased) in regions where the error is estimated to be below (above) its average value [10, 11, 12]. For finite element discretizations, this estimates can be based on the interpolation error [13, 14, 15, 16]. In fluid-dynamic problems, local mesh adaptation indicators are often functions of relevant flow variables, such as the density, the pressure, the Mach number or the velocity and on their first- and second-order derivatives. The underlying assumption

*Corresponding author
Email address: barbara.re@polimi.it (B. Re)

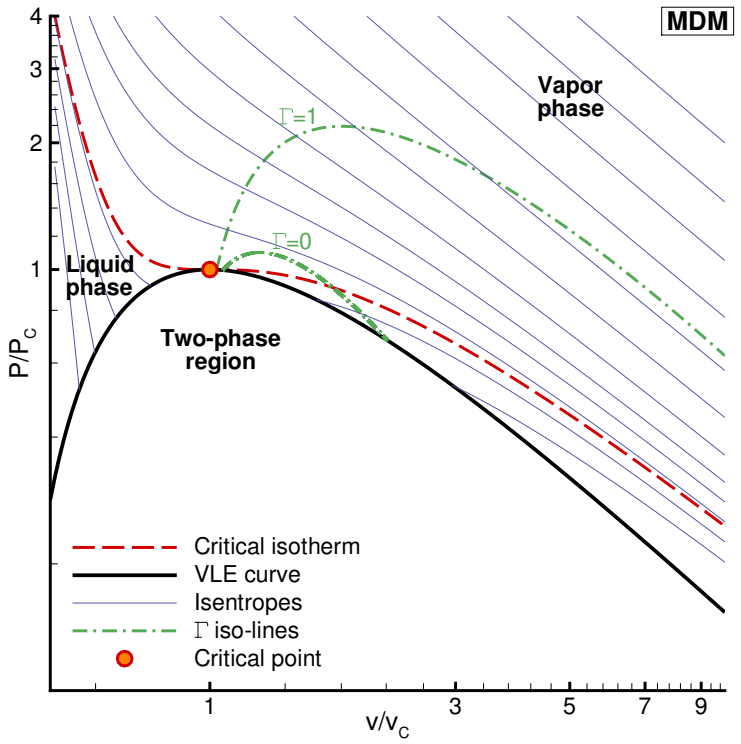

Figure 1: Representative isentropes and liquid-vapor saturation curve in the v-P plane in the non-ideal compressible-fluid region for the siloxane MDM under the polytropic van der Waals gas. The critical isotherm, the critical point and iso-lines of the fundamental derivative of gasdynamics Γ [22] are also shown.

of this approach is that the largest error occurs in the regions of the domain where the solution changes most rapidly, therefore the grid spacing is reduced where the gradients are large, while it is increased where the solution is smooth. Thanks to their simplicity and fast computation, this kind of adaptation criteria is widely and successfully used in various fluid-dynamics problems [17, 18, 19].

The main drawback of the adaptive indicators based on flow variables is that the optimal indicator for the problem under investigation, i.e. the variable (or combination of variables) that allows to efficiently detect the relevant flow structures, is usually problem-dependent. However, some general assumptions can be stated on the based of the expected flow behavior, as for instance the presence of shock waves, vortex structures or rarefaction fan. In this regards, since the relationships among the diverse flow variables strongly depend on the assumed thermodynamic model, the selection of the proper error indicator is not straightforward if the fluid thermodynamics depart from the well-known ideal-gas conditions, for which a wealth of literature regarding the effectiveness of the error indicators is already available [2, 3, 20]. The above is indeed the case for the so-called non-ideal compressible-fluid dynamics (NICFD), the branch of fluid dynamics devoted to the study of compressible fluids in the vicinity of the liquid-vapor saturation curve and critical point, see Figure 1. In NICFD, non-ideal thermodynamics results in large compressibility of the fluid, non-ideal dependence of the speed of sound on the density, critical point phenomena, phase transition. For fluid characterized by large molecular complexity, non-classical gasdynamics behavior is possibly observed [21]. Therefore, the applicability of mesh adaptation criteria derived for the constant-specific-heat ideal-gas case is questionable in these highly non-ideal flow conditions.

The present work is a first, tentative assessment of local mesh adaptation criteria for steady two-dimensional NICFD under the inviscid assumption. To this purpose, numerical simulations of supersonic under-expanded nozzle jets of nitrogen and siloxane MDM operating close to the liquid-vapor saturation curve are performed to study the effectiveness of different adaptation criteria. These include combinations

of the gradient and the Hessian of the pressure, the Mach number, the density and the temperature, within a multi-passage adaptation strategy that allows to detect weaker phenomena [23]. Moreover, given the nature of the flow, also anisotropic mesh adaptation is exploited [11, 24]. The van der Waals thermodynamic model is used to take into account, at least qualitatively, non-ideal compressible-fluid effects, which are observed in the proximity of the critical point.

Under-expanded jets represent a valuable benchmark for mesh adaptation techniques because of the complex flow structure, including oblique and normal shock waves, supersonic expansions and shear discontinuities. Besides their unique fluid dynamics features, under-expanded supersonic jets of gases are of relevant interest also in several technical applications, including for instance particle nucleation, turbomachinery, exhaust plumes of propulsion systems, high-pressure gas discharge, fuel injectors, laser cutting with assist gas. Reference [25] gives a review of experimental studies as well as numerical investigations of under-expanded jets of ideal gases with constant isochoric specific heat.

The ideal gas thermodynamic model provides accurate estimation of gas properties only if thermodynamic conditions are sufficiently away from the vapor-liquid saturation curve and from the critical point. Recent applications require however the working fluid to operate within the non-ideal compressible-fluid region, where the thermodynamic behavior of the substance deviates significantly from the ideal one, see Figure 1. In such conditions, fluid transport and physical properties exhibit a peculiar dependence on the pressure and temperature, which can be exploited in certain industrial processes. For example, under-expanded jets of supercritical CO_2 are widely used in the pharmaceutical industry and in food processing in order to product micro- or nano-particles [26, 27]. In Organic Rankine Cycle (ORC) engines, organic fluids of high molecular complexity are used as working fluids in the Rankine cycle for low-temperature renewable-energy sources [28]. This technology has been successfully used to recover waste heat and to exploit geothermal, biomass and solar sources [29]. As reported in Reference [30], highly under-expanded jets can occur between turbine blades if supercritical ORCs operate in off-design conditions.

Simulations of so-called real-gas under-expanded jets were carried out by Obayashi [31], who considered the thermal imperfection in combination with the ideal gas model in order to take into account the real gas effects of the exhaust plumes of the Space Shuttle propulsion system. To investigate gas non-ideality or caloric imperfection, Guardone and co-workers [32] performed numerical simulations of under-expanded jets of nitrogen gas in supercritical conditions using a finite volume scheme for non-ideal gases. The fluid thermodynamics was modeled by means of the polytropic van der Waals approximation. In the dilute gas regime, the results in [32] agree fairly well with the experimental results of Katanoda and co-workers [33, 34].

In the present work, the `FlowMesh` code, currently under development at the Department of Aerospace Science and Technology of Politecnico di Milano, is used to solve the flow equations under non-ideal thermodynamics. The code implements an unstructured-grid finite-volume scheme based on an innovative interpretation of grid elements modifications due to mesh adaptation within the Arbitrary Lagrangian-Eulerian (ALE) framework [35, 36, 37], which guarantees the scheme to be conservative by construction. The VThermo library, now included in FluidProp [38], is used to compute the fluid thermodynamics. Local grid adaptation techniques, such as node movement (r-refinement) and node insertion/deletion (h-refinement) techniques, are employed to locally modify the computational grid to reach a variable grid spacing, avoiding a complete re-meshing of the domain [2, 4]. To efficiently modify unstructured triangular grids, especially when performing anisotropic adaptation, the flow solver has been linked to the automatic re-mesher `Mmg` [39].

The paper is structured as follows. Section 2 briefly describes the numerical method and the thermodynamic model. Section 3 details the considered mesh adaptation techniques and reports on the results of a simple shock reflection problem to assess the solution procedure. Section 4 presents the results for under-expanded jets of non-ideal compressible fluids with different adaptation strategies. Finally, in Section 5, final considerations are drawn regarding the suitable adaption criteria for non-ideal compressible-fluid flows.

Polytropic ideal gas	Polytropic van der Waals gas
$P(T,v) = \frac{RT}{v}$	$P(T,v) = \frac{RT}{v-b} - \frac{a}{v^2}$
$e(T,v) = \frac{T}{\delta}$	$e(T,v) = \frac{T}{\delta} - \frac{a}{v}$
$\Pi(\mathsf{u}) = \delta \left[E^{\mathrm{t}} - \frac{\lvert\boldsymbol{m}\rvert^2}{2\rho}\right]$	$\Pi(\mathsf{u}) = \delta \frac{E^{\mathrm{t}} - \lvert\boldsymbol{m}\rvert^2/(2\rho) + a\rho^2}{1-b\rho} - a\rho^2$

Table 1: Polytropic ideal gas and van der Waals thermodynamic models. δ is the inverse dimensionless specific heat at constant volume, namely, $\delta = R/c_v$, which is constant under the polytropic assumption. The van der Waals constants a and b are specifics of the fluid and are related to the critical temperature T_{C} and pressure P_{C}, namely $a = 27/64\, R^2\, T_{\mathrm{C}}^2/P_{\mathrm{C}}$ and $b = 1/8 R\, T_{\mathrm{C}}/P_{\mathrm{C}}$.

2. Physical model and solution method

2.1. Flow equations

The governing equations for a compressible inviscid fluid in two spatial dimensions are provided by the unsteady Euler equations, which read

$$\frac{d}{dt}\int_{\mathcal{C}} \mathsf{u}\, d\boldsymbol{x} + \oint_{\partial\mathcal{C}} \mathbf{f}\left(\mathsf{u}\right)\cdot\boldsymbol{n}\, ds = 0 \qquad\qquad \forall \mathcal{C} \subseteq \Omega \tag{1}$$

where $\boldsymbol{x} = (x, y)^{\mathrm{T}}$ is the position vector, t is the time and $\mathsf{u} = (\rho,\, \boldsymbol{m},\, E^{\mathrm{t}})^{\mathrm{T}} \in \mathbb{R}^+ \times \mathbb{R}^3$ is the vector of conservative variables, composed by the density ρ, the momentum vector $\boldsymbol{m}$ and the total energy per unit volume E^{t}. The flux function is defined as

$$\mathbf{f}(\mathsf{u}) = \left(\boldsymbol{m},\ \boldsymbol{m}\otimes\boldsymbol{m}/\rho + \Pi(\mathsf{u})\mathbf{I}^2,\ \left[E^{\mathrm{t}} + \Pi(\mathsf{u})\right]\boldsymbol{m}/\rho\right) \in \mathbb{R}^4 \times \mathbb{R}^2 \tag{2}$$

where $\mathbf{I}^2$ is the 2×2 identity matrix and $\Pi(\mathsf{u}) = \Pi(\rho, \boldsymbol{m}, E^{\mathrm{t}})$ is the pressure function, whose analytical expression depends on the adopted thermodynamic model. The solution is sought for in the spatial domain $\Omega \in \mathbb{R}^2$ for all times $t \in \mathbb{R}^+$. The arbitrary control volume $\mathcal{C} \in \Omega$ is bounded by the surface $\partial\mathcal{C}$. The vector $\boldsymbol{n}(s) \in \mathbb{R}^2$ is the outward unit normal to the boundary $\partial\mathcal{C}$ and it is a function of the curvilinear coordinate s along the boundary itself. In the following equations, the variables of integration $d\boldsymbol{x}$ and ds are omitted for conciseness. Suitable initial and boundary conditions are to be specified on the boundary $\partial\Omega$ to obtain a well-posed problem, [40].

2.1.1. Thermodynamic model

In the present work the polytropic van der Waals model is used to derive the functional form of the pressure function $P = \Pi(\mathsf{u})$. The thermal and caloric Equation of State (EoS) and the pressure function Π are reported in Table 1, along with the ones of the polytropic ideal gas model. The polytropic van der Waals model is the simplest thermodynamic model capable of taking into account, at least qualitatively, the non-ideal compressible-fluid effects [41].

According to the ideal gas model, the isotherms are hyperbolae in the volume-pressure (v-P) thermodynamic plane, namely, $P(T, v) = RP/v$, where v is the volume for unit mass, T is the temperature and R is the gas constant. On the contrary, the isotherms in non-ideal conditions exhibit different shapes depending on the thermodynamic state. With reference to Figure 1, the isotherms of van der Waals fluids tend to ideal-gas hyperbolae at high temperature, but become steeper close to the vapor-liquid saturation curve, namely, in the so-called non-ideal compressible-fluid region [42]. A quantitative measure of non-ideal behavior is the so-called compressibility factor Z, defined as

$$Z(T, v) = \frac{P(T, v)\, v}{RT}\,. \tag{3}$$

Since $Z = 1$ for the ideal gas, a value different from unity indicates a deviation from ideal gas behavior.

2.2. Finite volume solution of the flow equations

The finite volume discretization is applied to solve Eq. (1) supplemented with the thermodynamic models in Section 2.1.1. The spatial domain Ω is split into N_m non-overlapping finite volumes $\mathcal{C}_i \in \Omega$, such that $\bigcup_i \mathcal{C}_i \equiv \Omega$. The resulting set made by the nodes of the triangulation is labeled $\mathcal{K}$. For each finite volume, the discrete counter part of Eq. (1) reads

$$\frac{d\left[V_i \mathsf{u}_i\right]}{dt} = -\oint_{\partial\mathcal{C}_i} \mathbf{f}\left(\mathsf{u}\right) \cdot \boldsymbol{n}_i \qquad\qquad \forall i \subseteq \mathcal{K} \tag{4}$$

where u_i is the average value of u over $\mathcal{C}_i$, V_i is the area of $\mathcal{C}_i$ and $\boldsymbol{n}_i = \boldsymbol{n}_i(s)$ denotes the outward normal to the finite volume boundary $\partial\mathcal{C}_i$. The right-hand side of the previous equation is rearranged to separate the domain and the boundary contributions, i.e.

$$\oint_{\partial\mathcal{C}_i} \mathbf{f}\left(\mathsf{u}\right) \cdot \boldsymbol{n}_i = \sum_{k \in \mathcal{K}_{i,\neq}} \int_{\partial\mathcal{C}_{ik}} \mathbf{f}\left(\mathsf{u}\right) \cdot \boldsymbol{n}_i + \int_{\partial\mathcal{C}_i \cap \partial\Omega} \mathbf{f}\left(\mathsf{u}\right) \cdot \boldsymbol{n}_i \,, \tag{5}$$

where $\mathcal{K}_{i,\neq}$ is the set of the indices of the finite volumes $\mathcal{C}_k$ sharing a part of their boundary with $\mathcal{C}_i$, excluding i, i.e. $\mathcal{K}_{i,\neq} = \{k \in \mathcal{K}, k \neq i \mid \partial\mathcal{C}_i \cap \partial\mathcal{C}_k \neq \emptyset\}$, and $\partial\mathcal{C}_{ik} = \partial\mathcal{C}_i \cap \partial\mathcal{C}_k$ is the so-called cell-to-cell interface.

Introducing a suitable integrated numerical flux $\Phi \in \mathbb{R}^4$, to model the flux across the cell interface, and Φ^∂, for the boundary counterpart, Eq. (5) can be approximated as

$$\oint_{\partial\mathcal{C}_i} \mathbf{f}\left(\mathsf{u}\right) \cdot \boldsymbol{n}_i \simeq \sum_{k \in \mathcal{K}_{i,\neq}} \Phi(\mathsf{u}_i, \mathsf{u}_k, \boldsymbol{\eta}_{ik}) + \Phi^\partial(\mathsf{u}_i, \boldsymbol{\xi}_i) \,, \tag{6}$$

where the $\boldsymbol{\eta}_{ik}$ and $\boldsymbol{\xi}_i$ are the integrated outward normal to the interface $\partial\mathcal{C}_{ik}$ and to the i-th boundary portion respectively, i.e.

$$\boldsymbol{\eta}_{ik} = \int_{\partial\mathcal{C}_{ik}} \boldsymbol{n}_i \qquad \text{and} \qquad \boldsymbol{\xi}_i = \int_{\partial\mathcal{C}_i \cap \partial\Omega} \boldsymbol{n}_i \,. \tag{7}$$

To obtain accurate solutions and a non-oscillatory behavior around discontinuities, a high-resolution Total Variation Diminishing (TVD) expression for the numerical fluxes is used. In particular, a second-order centered scheme is blended to the first-order monotonicity-preserving Roe's scheme [43] through the van Leer slope limiter [44], to obtain a spatial accuracy between first- and second-order. In the present work the focus is on steady-state solutions of Eq. (1). The time term is thus dropped and a standard Newton-Krylov technique is used with defect correction to integrate the solution [45].

After every adaptation step, steady-state computations are restarted from an initial guess which is obtained by interpolating the old solution over the new grid with the ALE technique for unsteady computations described in [35, 36]. In the case of steady-state computations of interest here, this method simplifies to an area-weighted interpolation, which allows to locally conserve the solution.

3. Mesh adaptation

The present section details the grid modification procedure aimed at equi-distributing the numerical error over the computational domain, without excessively increasing the computational cost. The first step consists in building a target grid spacing on the basis of a local solution-based error estimator E, computed with the expressions given in Section 3.1. Then, the computational grid is modified by means of local operations, that includes node insertion through edge or element split, node deletion, edge swap and node-relocation.

3.1. Target grid spacing

As stated above, the grid spacing is modified according to error estimators expressed as functions of first- and second-order derivatives of suitable flow variables [2]. In the present work, different error estimators are compared, combining the gradient $\boldsymbol{\nabla} a$ and the Hessian matrix $\mathcal{H}(a)$ of a given quantity a of interest, e.g. pressure, Mach number, density, and temperature. To this purpose, suitable approximations of these differential operators are required. By applying the Gauss theorem to the finite-volume representation of the unknowns, the gradient of a scalar variable a on the generic node i is approximated as

$$\boldsymbol{\nabla} a_i \simeq \frac{1}{V_i} \left[\sum_{k \in \mathcal{K}_{i,\neq}} \frac{a_i + a_k}{2} \, \boldsymbol{\eta}_{ik} + a_i \boldsymbol{\xi}_i \right] . \tag{8}$$

The Hessian matrix is computed by applying twice the previous discrete gradient operator. As suggested in [46, 14], the error estimator based on the Hessian matrix is scaled with respect to the gradient to reduce the predominance of the strongest phenomena, like shock wave, over weak flow features. Moreover, a further estimator, defined in the following *complex Hessian*, is built adding to the modified Hessian a term proportional to the gradient to obtain a more uniform refinement near flow variations. With this regard, consider for instance a step-like variation that on the initial grid is spread over some elements. Since the gradient has opposite sign at the two extremes, the second derivative goes to zero in the central part of the variation. Thus, this region will not be refined if an indicator proportional only to the Hessian matrix is used. To avoid this drawback the following estimator can be used

$$\mathcal{H}^{\star}(a) \simeq \frac{\ell^2 \, |\text{second derivative}|}{\ell \, |\text{first derivative}| + \epsilon \, |\mu|} + \frac{\ell \, |\text{first derivative}|}{\ell^2 \, |\text{second derivative}| + \epsilon \, |\text{mean value}|} \tag{9}$$

where ℓ is the local mesh size and the term $\epsilon \, |\text{mean value}|$ acts as a filter to avoid the refinement of the smallest oscillations [46]. The constant ϵ is a number less 1 and in this work it is set equal to 0.12.

When a simple isotropic adaptation is performed, a single scalar estimator E_i is required. In this case, the value of E_i is computed, according to the chosen error estimator, as the norm of the gradient or as the module of the two vectors obtained by projecting the Hessian matrix along the direction parallel and perpendicular to the local velocity, respectively,

$$E_i(a) = V_i \sqrt{E(\hat{\boldsymbol{\tau}}, a)^2 + E(\hat{\boldsymbol{\zeta}}, a)^2} \qquad \text{where} \qquad E(\mathbf{p}, a) = \mathbf{p}^{\mathrm{T}} \mathcal{H}(a) \mathbf{p} \, , \tag{10}$$

with $\mathbf{p}$ a generic vector, while $\hat{\boldsymbol{\tau}}$ and $\hat{\boldsymbol{\zeta}}$ are the unit-vectors respectively tangent and normal to the velocity. Finally, different estimators are averaged to form a *compound* error estimator.

The target isotropic grid spacing is computed from an initial couple of grid and solution. For each node of the grid, the average length ℓ_i of the connecting nodes is computed and the error E_i is estimated as described above. Then, the refinement and coarsening thresholds τ_R and τ_C are computed on the basis of the mean μ and the standard deviation σ of the error estimator E over all nodes. Theoretically, a uniform error distribution implies a null standard deviation at the end of the adaptation procedure, but, in practice, this is not computationally worthwhile. Thus, a good compromise consists in defining the refinement and coarsening thresholds as

$$\tau_R = \mu + k_R \sigma \qquad \text{and} \qquad \tau_C = k_C \mu \, , \tag{11}$$

where $k_R > 0$ and $0 < k_C < 1$ are user-defined parameters that allow to tune the refinement and coarsening. The target grid spacing, used to drive grid adaptation, is computed by specifying at each node the desired average length $\bar{\ell}_i$, which is lower than the actual length ℓ_i for the nodes with an error estimate $E_i > \tau_R$ and it is greater if $E_i < \tau_C$.

3.1.1. Multi-passage technique

A possible drawback of solution-based adaptation is that the refinement is over-focused on regions where the error peaks are located. For instance, if the flow field encloses both a shock wave and a smooth,

continuous rarefaction wave, the grid would probably be refined near the shock because it embeds the strongest gradients but it would remain unaltered (or over-coarsened) near the weaker feature. As suggested by Aftosmis [23], a multiple evaluation of the error estimation for each adaptation step could be applied to circumvent this problem. This technique, called in the following *multi-passage*, consists in re-computing at each passage the refinement and coarsening thresholds excluding the nodes already marked in the previous passages. For example, if in the first passage the threshold τ_{R1} is computed, in the second passage the mean and the standard deviation are evaluated excluding nodes with an error greater than τ_{R1}. In this way, the refinement threshold τ_{Rn} decreases at every passage allowing to capture also less intense features. Eventually, all nodes whose error is greater than the value τ_R computed in last passage are marked for refinement. In the grid coarsening step, the threshold τ_C is evaluated using the mean value computed in the last passage only. Since excluding the largest errors reduces the mean value, fewer elements are marked for coarsening in the multi-passage procedure than they are in the single-passage one.

3.1.2. Anisotropic adaptation

A different procedure is followed when anisotropic mesh adaptation is performed, since for the definition of the target grid spacing the edge size is not sufficient but also informations about element shape and orientation are required. To this end, a metric map $\mathcal{M}(\boldsymbol{x})$ is defined at each grid point on the basis of the Hessian matrix (or on the complex Hessian matrix). More precisely, $\mathcal{M}(\boldsymbol{x})$ is a 2×2 symmetric matrix defined as $\mathcal{M} = R\Lambda R^{-1}$, where R is the eigenvector matrix of the Hessian and Λ is a diagonal matrix containing a modified version of its eigenvalues λ_i to account for the desired error ε, namely $\Lambda = \mathrm{diag}\,\{c\,\lambda_1/\varepsilon, c\,\lambda_2/\varepsilon\}$ where c is a constant that for two-dimensional problems read $2/9$.

Thanks to this metric map, it is possible to specify at a grid node different target edge sizes in different directions. Indeed, the length of a vector $\boldsymbol{w}$ in terms of the metric map is defined as $\|\boldsymbol{w}\|_{\mathcal{M}} = \sqrt{\boldsymbol{w}^T\mathcal{M}\boldsymbol{w}}$. According to this definition, the geometric locus of all points P that lie at a distance h from the point O, i.e. that satisfy $\|P - O\|_{\mathcal{M}} = h$, is an ellipse [47].

3.2. Grid alteration procedure

The grid optimization procedure considered here allows to combine different adaptation techniques and to repeat the desired adaptation sequence for a certain number of cycles or until a specified threshold for the number of grid modifications is reached. A loop on all elements is performed to check if their edges comply with the target grid spacing. If an edge does not comply with the target grid spacing, a node can be inserted or removed to modify the edge size. After each modification, the local connectivity is re-built so that only triangular elements constitute the grid and no hanging nodes are present. In order to preserve the correct geometry of the domain, the boundaries are represented by spline curves that are used when the local modification involved a boundary node. Indeed, in case of boundary refinement the position of the new node is prescribed by the spline curve, while a boundary node is not removed if this leads to a significant deviation from the original boundary geometry.

In addition to node insertion and deletion, the adaptation sequence includes grid smoothing and edge swapping. These latter techniques are applied to improve the quality of the mesh from a geometrical point of view [1, 48]. For this reason, the element quality measure is not related to the error estimator, but it is defined as

$$Q_e = \max_{k\in\mathcal{K}_e}(\ell_k)\,\frac{1}{2}\sum_{k\in\mathcal{K}_e}\ell_k\Big/A_e \tag{12}$$

where A_e is the area of the triangle and ℓ_k is the length of k-th edge of the element and $\mathcal{K}_e$ is the set of its nodes. For an equilateral triangular element (maximum quality, minimum value of Q_e) one has $Q_e = 2\sqrt{3} \simeq 3.4641$. An edge is swapped between two adjacent elements if the quality of the element with the lowest quality is improved.

3.3. Regular shock reflection in dilute gas conditions

The simple, regular reflection of a shock wave over a wall was simulated under the polytropic ideal gas assumption with a specific heats ratio $\gamma = 1.4$, to verify the performances of the foregoing adaptation

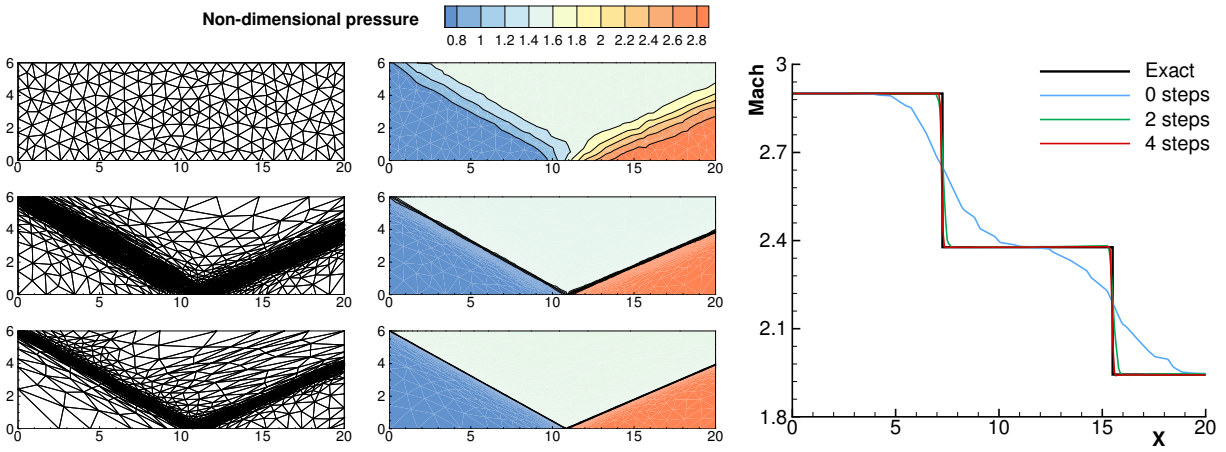

Figure 2: Regular shock reflection results. Left and center: computational grids and pressure contour plots at three different adaptation steps. Pressure is made dimensionless by means of the reference pressure $P_{\text{ref}} = 1\,\text{atm}$. From top to bottom: original grid (241 nodes, 420 elements), grid after 2 adaptation cycles (2 454 nodes, 4 797 elements), final grid at 4-th adaptation level (2 845 nodes, 5 589 elements). Right: Mach number along the line $y = 2.0$ obtained on the three grids and the exact solution.

strategy. The computational domain is a rectangular unstructured mesh with a wall at the bottom. The initial solution consists in a uniform flow at Mach $M = 2.377$ and incidence $\alpha = -10.95°$. On the left boundary a flow parallel to the wall at Mach $M = 2.9$ is enforced. The steady state is a flow parallel to the wall with an oblique shock, which is reflected at the wall as a shock with different intensity. Therefore, the flow appears as divided into three separate uniform regions: before the first shock, downstream the reflected shock and between two waves.

The initial grid is a uniform coarse unstructured grid, made of 241 nodes and 420 triangles. The error estimator is based on the Hessian of the pressure and an anisotropic grid adaptation is performed. Four adaptation steps are required to reach convergence of the adaptation process, with $\varepsilon = 1.0 \times 10^{-4}$. The computational grids and the ones obtained after 2 and 4 adaptation cycles are shown along with the solutions in Figure 2. As expected, the accuracy of the solution increases with adaptation cycles. An excellent agreement between the profile of the Mach number along the line $y = 2.0$ over the final grid and the exact solution is achieved.

4. Grid adaptation in non-ideal compressible-fluid flows

Numerical simulations were performed to investigate the impact of different solution-based adaptation criteria on the solution of under-expanded nozzle jets of nitrogen and of the siloxane MDM in non-ideal compressible-fluid region. The expected flow features are depicted in Figure 3 and include all flow features that can be of interest for assessing the adaptation procedure, namely, strong and weak shock waves, slip lines and rarefaction fans. If a supersonic jet exits from a nozzle at a pressure higher than the ambient one, the jet is said to be under-expanded and the expansion process continues outside the nozzle. As a consequence, a Prandtl-Meyer expansion fan forms, centered at the nozzle edge. A constant-pressure slip line detaches from the nozzle edge and it separates the jet flow from the quiescent gas. As sketched in Figure 3, the expansion fan is reflected at the jet symmetry axis and then it intersects the slip line. From the slip line, the rarefaction fan is reflected as an isentropic compression fan. Propagating downstream, compression waves coalesce into an oblique intercepting shock, which is reflected at the symmetry axis. If the jet is highly under-expanded, i.e. the ratio between the exit pressure and the ambient one is sufficiently large, a normal shock, called Mach disk, occurs and a subsonic region is observed near the centerline. The Mach disk ends at a triple point, where a slip line is formed that separates the supersonic region (behind the reflected oblique shock) from the subsonic one. In axisymmetric flows, the interception shock and the

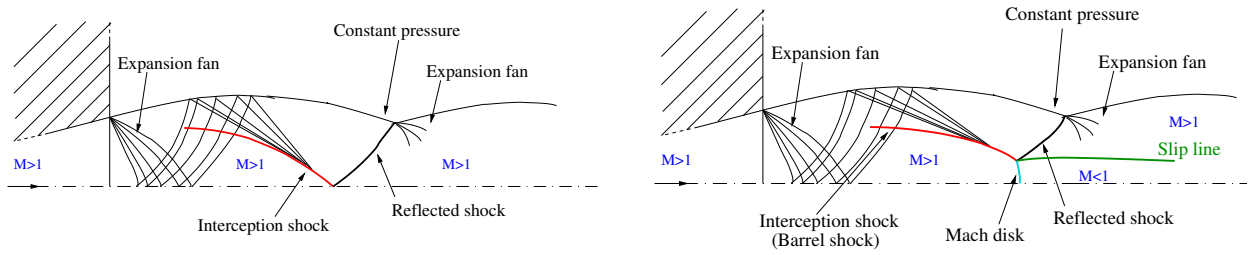

Figure 3: Left: weakly under-expanded jet. The interception shock is reflected as an oblique shock and the flow downstream is therefore supersonic. This configuration is referred to as a regular reflection (RR). Right: Mach reflection (MR) of a highly under-expanded jet with Mach disk formation. Downstream of the triple point, a slip line separates the subsonic flow near the jet-center (downstream of the normal shock) from the outer region of the flow at supersonic speed.

Mach disk form the so-called barrel shock configuration. Downstream the Mach disk, the jet shape, namely the position of the slip line, is modified by a complex flow structure due to further shock interactions.

The computational domain is described in Section 4.1, along with the procedure to compute the boundary conditions for the tested operating conditions. Since the present work aims at investigating the flow structure downstream of the supersonic exit section of the nozzle, only this latter region is simulated. A reference solution is first computed for both fluids in Section 4.2. Then, different error estimators are evaluated for the nitrogen flow in Section 4.3 to identify the most suitable for under-expanded jets in non-ideal compressible-fluid region. Finally, the results for the MDM jet are presented in Section 4.4.

4.1. Setup of numerical simulations

The computation domain is a $30L \times 10L$ rectangular grid composed by triangular elements, with L the size of the nozzle exit section. Five numerical boundaries are defined. The left side is made by half of the nozzle exit section ($x = 0, 0 \leq y \leq 0.5L$), which in the computational domain of the jet is in fact a supersonic inlet, and by a solid wall ($x = 0, y > 0.5L$). The flow is symmetric with respect to the lower boundary ($y = 0$), which represents the jet center-line. The nozzle discharges in quiescent atmosphere, so constant ambient pressure is enforced along the upper boundary ($y = 10L$). Non-reflecting boundary conditions are imposed on the right boundary ($x = 30L$) since both supersonic and subsonic flow regions are possibly observed.

The quasi mono-dimensional theory is used to compute the inflow boundary conditions at the nozzle exit, which depend on the stagnation or reservoir state (pressure and temperature) of the gas and the ambient pressure. The operating conditions, obtained with the van der Waals and the ideal gas model, are shown in the thermodynamic plane P-v in Figure 4 and detailed in Table 2. The subscripts 0, e and a indicate respectively variables in the reservoir, on the exit section and the ambient ones. Flow variables are reduced with respect to their critical values, i.e. scaled by $T_C = 126.192$ K and $P_C = 3.396$ MPa for nitrogen and $T_C = 564.1$ K and $P_C = 1.415$ MPa for MDM. In all tests, the reduced ambient pressure is equal to 0.2 and the pressure ratio between the reservoir and the ambient is 12.5. The critical pressure is enforced on the nozzle exit section. Flow quantities at the exit section, including the Mach number reported in Table 2, are computed according to the one-dimensional theory of gasdynamics nozzle under the assumption of isentropic flows at constant total specific enthalpy [49]. The polytropic van der Waals thermodynamic model is used with the ratio of the specific heats at constant pressure and volume γ equal to 1.4 for nitrogen and 1.0173 for MDM.

For nitrogen vapor, an isentropic expansion that ends very close to the saturation curve is chosen by setting $v_a/v_C = 8.0$. Thus, the expansion from the nozzle exit till the ambient occurs in the non-ideal compressible-fluid region, as indicated also by the compressibility factor at the exit section $Z_e = 0.771$. However, despite this value, the deviation between the expansions obtained with the two different thermodynamic models shown in Figure 4 is not much significant. This can be explained by the fact that nitrogen gas consists of simple molecules.

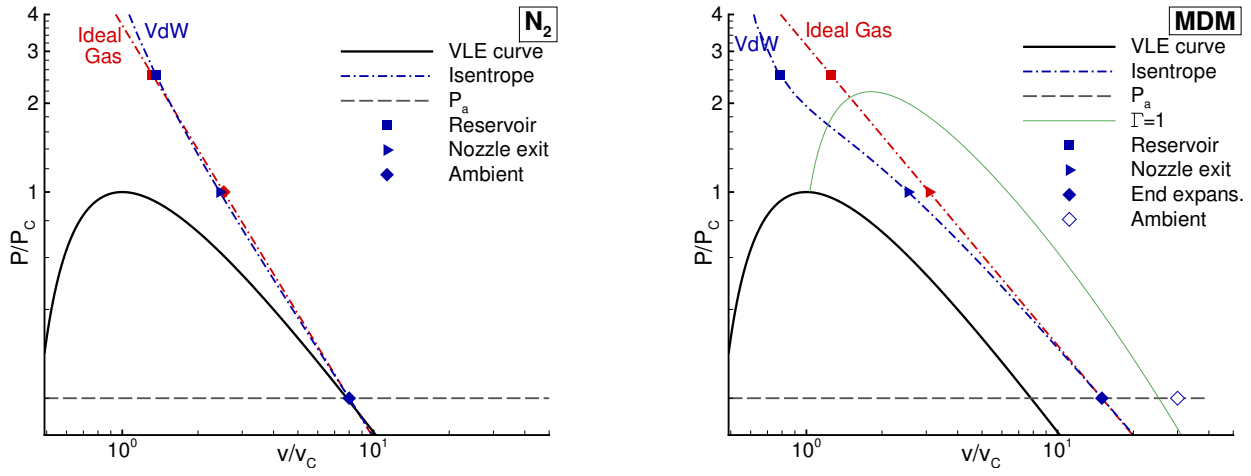

Figure 4: Operating conditions of under-expanded nitrogen (left) and MDM (right) jets in the thermodynamic plane P/P_C-v/v_C. The nozzle discharges at an ambient pressure $P_a/P_C = 0.2$. The reservoir, the nozzle exit section (which is the boundary condition for the numerical simulation) and the ambient conditions defined in Table 2 are shown, along with the isentropes along which the nozzle expansions take place. Both the expansions obtained with the van der Waals and the ideal gas model are shown. For the MDM jet, the ambient conditions are imposed in the simulations to enforce a jump in entropy between the jet and the ambient. Indeed, the full symbol ◆ indicates the end of the expansion under the isentropic hypothesis, while the empty symbol ⋄ indicates the enforced ambient conditions.

	Reservoir		Nozzle exit				Ambient		Expansion	
	P_0/P_C	v_0/v_C	P_e/P_C	v_e/v_C	M_e	Z_e	P_a/P_C	v_a/v_C	P_0/P_a	v_0/v_a
N_2 VdW	2.50	1.359	1.0	2.44	1.226	0.771	0.2	8.00	12.5	0.170
N_2 Id.G.	2.50	1.317	1.0	2.53	1.223	1.000	0.2	8.00	12.5	0.165
MDM VdW	2.50	0.782	1.0	2.54	1.409	0.786	0.2	15.00	12.5	0.052
MDM Id.G.	2.50	1.253	1.0	3.08	1.347	1.000	0.2	15.00	12.5	0.084

Table 2: Operating conditions of isentropic under-expanded nitrogen and MDM jets. Flow variables are scaled with respect to their critical values, i.e. $T_C = 126.192$ K, $P_C = 3.396$ MPa for nitrogen and $T_C = 564.1$ K, $P_C = 1.415$ MPa for MDM.

Differently from the nitrogen gas, the siloxane MDM is a high molecular complexity fluid. Indeed, it allows a region in the thermodynamic plane where the fundamental derivative of gasdynamics Γ, defined as

$$\Gamma = 1 + \frac{\rho}{c}\left(\frac{\partial c}{\partial \rho}\right)_s = \frac{v^3}{2c^2}\left(\frac{\partial^2 P}{\partial v^2}\right)_s , \tag{13}$$

exhibits values less than 0, see Figure 1, indicating that non-classical gasdynamic phenomena may occur [22]. To avoid to entering the region of $\Gamma < 0$, where the peculiar thermodynamic behavior makes difficult to reach the convergence in numerical simulations, for the MDM jet the ambient volume is set to $v_a/v_C = 15$, so that the expansion from the exit section to the ambient takes place within the region where $0 < \Gamma < 1$. In this region, the speed of sound, differently from ideal gases, decreases on isentropic compressions and increases in isentropic expansions. Moreover, in quasi-mono-dimensional steady flows, the decrease in speed of sound is overcompensated by the increase in local velocity and a non-monotone variation between Mach number and density may be observed in supersonic regimes [22]. Due to the strong non-ideal gas effects that occur in this region, the deviation between the expansion predicted by the van der Waals model and the one predicted by the ideal gas model is pronounced, as displayed in Figure 4. Finally, a jump in entropy between the jet and the ambient is enforced by imposing a different value of the ambient density, namely it is imposed $v_a/v_C = 30$.

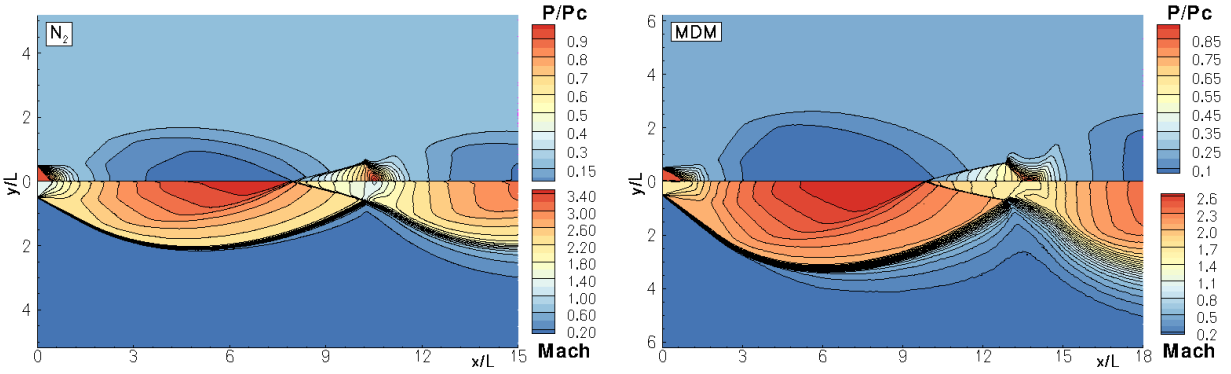

Figure 5: Reduced pressure (top) and Mach number (bottom) contour plots of the reference solutions. Left: nitrogen jet, right: MDM jet

4.2. Reference solution and flow description

A reference solution was computed for the nitrogen and MDM jet over a fine grid of 86 381 nodes and 257 858 elements. Grid elements have smaller sizes in the bottom part of the grid, where the largest gradients of the solutions are expected. In Figure 5 the pressure and the Mach contours are shown above and below the symmetry line, respectively. As expected, a Prandtl-Meyer expansion is observed at the nozzle exit, which is reflected along the symmetry axis and the slip line. The resulting compression wave coalesces into an interception shock which produces a Regular Reflection (RR) at the symmetry axis. The most significant features of the flow, i.e. the constant-pressure line which separates the jet from the ambient fluid and the shock reflection which takes place at jet center line around $x/L = 8$ for nitrogen and $x/L = 10$ for MDM, are well captured. Another relevant feature is the interaction between the constant-pressure line and the reflected shock, which occurs very close to the symmetry axis and results in a strong rarefaction wave being reflected towards the axis. Note that the flow downstream of the triple point is not investigated because the viscosity plays a major role in momentum transfer [33], therefore flow features cannot be correctly captured under the inviscid approximation considered here.

4.3. Assessment of mesh adaptation criteria in the nitrogen jet flow

In the case of adaptive simulations a low accuracy initial solution is first computed to start the solution process. First the solution is computed using the first-order upwind scheme and a preliminary grid adaptation is carried out on this solution, resulting in a grid composed by 8408 nodes and 24629 triangular elements. This solution is used as the initial condition in the following high-resolution computations.

Three different sections at constant x are selected to compare the density and Mach profiles obtained in different simulations. These sections, depicted in Figure 6, are located: (A) near the exit section where the Prandtl-Meyer expansion takes place, (B) near the section of maximum width of the jet and (C) across the reflected shock.

First, simple error estimators based on one variable only are compared. The Hessian of pressure, Mach number, density and the gradient of the last two are tested to drive the adaptation, with $k_R = 2.5$ and $k_C = 0.25$. Figure 6 shows the density and the Mach number profiles obtained after three adaptation steps. The expansion fan ($0 \leq y/L \leq 0.6$ at $x/L = 0.25$) is well captured by all the estimators, especially by the Hessian of the pressure, which leads to the higher, i.e. more similar to the reference one, maximum value of the density at the end of the expansion. However, as expected, the Hessian of the pressure does not allow to detect the slip line, since it separates two regions at the same pressure, but it leads to a correct detection of the rarefaction fan. Despite all estimators produce an insufficient refinement at the slip line, probably due to an insufficient number of adaptation steps, the estimators based on the gradient of density and Mach number produce the minimum deviation from the reference density profile, as it can be observed at $x/L = 5$. The region of the grid near the reflected shock ($x/L = 9$) is not adequately refined, since the

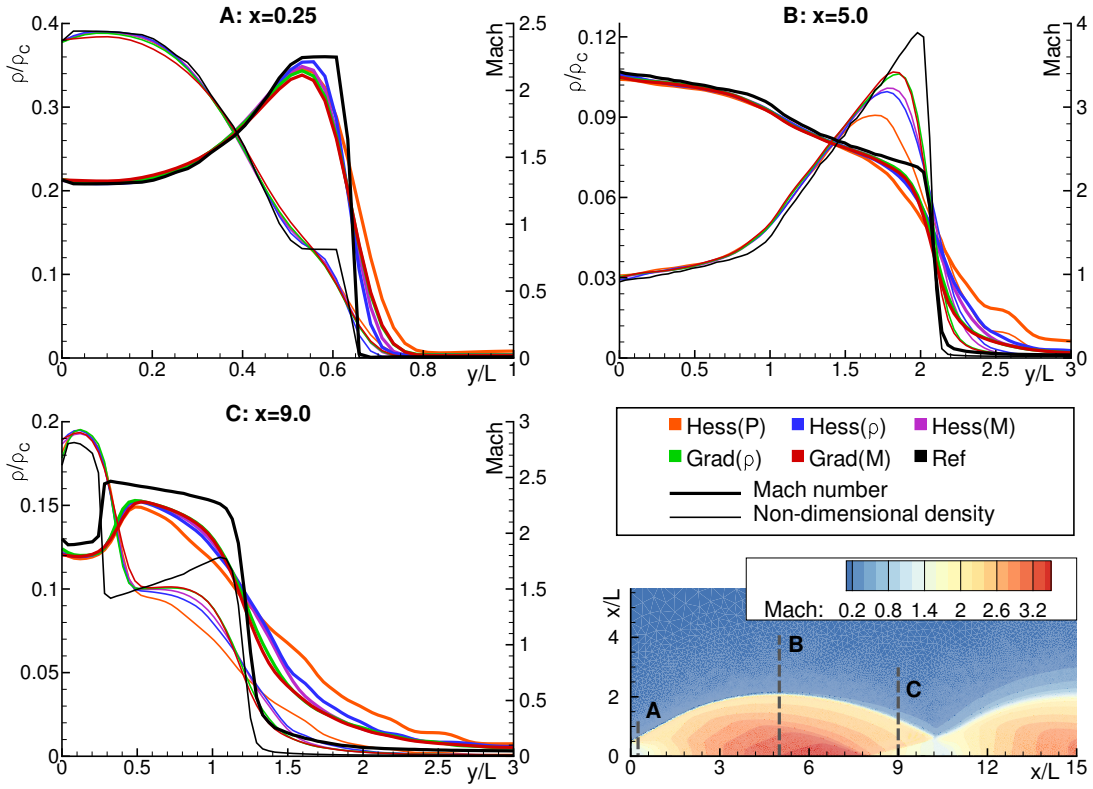

Figure 6: Comparison of the results for the nitrogen jet obtained with different estimators after 3 adaptation steps, using 2 multi-passages. In the legend, grad and Hess indicate respectively the gradient and the Hessian operator, Ref is the reference solution. Reduced density and Mach number are shown along three lines at three different positions across the jet center line.

solutions obtained after 3 steps—similar for all estimators—are very different from the reference one. In all sections, no significant deviation between the results obtain with the estimators based on the density and the ones based on the Mach number is observed.

According to the previous results, a combination of different estimators should be exploited to accurately capture all the relevant flow features. The Hessian of the pressure allows to better capture shock waves since the pressure is continuous across the slip line. Thus, it is combined with the gradient of the Mach and of the density, which perform better than the others in detecting the slip line. Moreover, since the flow features present in the jet have different intensities, the multi-passage technique, described in Subsection 3.1.1, is exploited and 5 re-computations of the refinement and coarsening thresholds are performed.

Figure 7 shows how the solution changes after different adaptation steps (from 3 to 10) using the estimators $\mathcal{H}(P)+\nabla\rho$ and $\mathcal{H}(P)+\nabla M$ respectively, with $k_R = 2.5$ and $k_C = 0.25$. It can be observed that, even with the compound estimators and 5 multi-passage, three adaptation steps are not sufficient to well resolve all the flow features. Eight steps proved to be sufficient to obtain convergence of the adaptation procedure, i.e. to obtain a computational grid which satisfies the imposed level of error uniformity (k_C and k_R). The number of grid nodes is 27 152 nodes and 29 473 nodes for eight adaptation steps for the estimator $\mathcal{H}(P)+\nabla\rho$ and $\mathcal{H}(P)+\nabla M$ respectively. No significant differences between the two compound estimators are observed and both produces results that are in good agreement with the reference ones. It should be highlighted that, because of linearity of the associated characteristic field, slip lines are extremely hard to capture using an artificial viscosity numerical scheme, such as the Roe scheme used here to capture non-linear shock waves. The grid adaptation procedure allows to attain an acceptable level of spatial resolution around the slip line, thus reducing the effect of numerical viscosity.

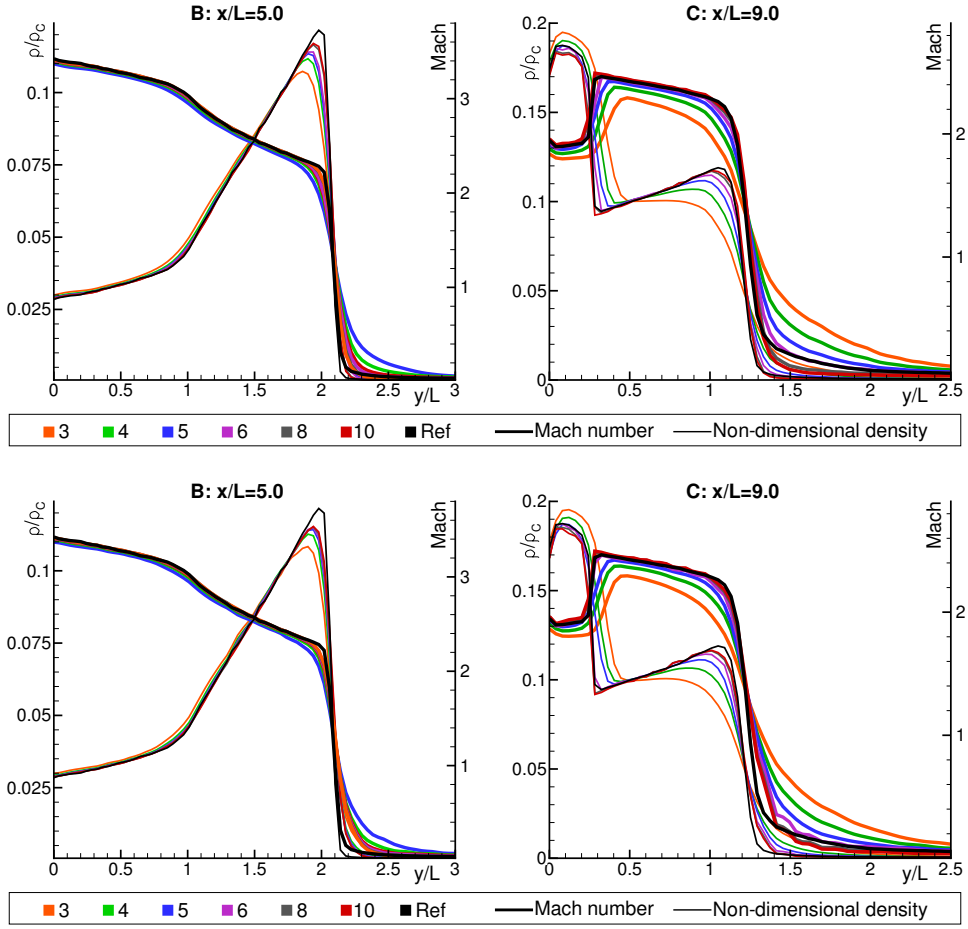

Figure 7: Solutions for the nitrogen jet obtained using the estimator $\mathcal{H}(P) + \nabla M$ (top) and $\mathcal{H}(P) + \nabla \rho$ (bottom) and 5 multi-passages at different adaptation steps (from 3 to 10). Reduced density and Mach number are shown at two different positions along the jet center line.

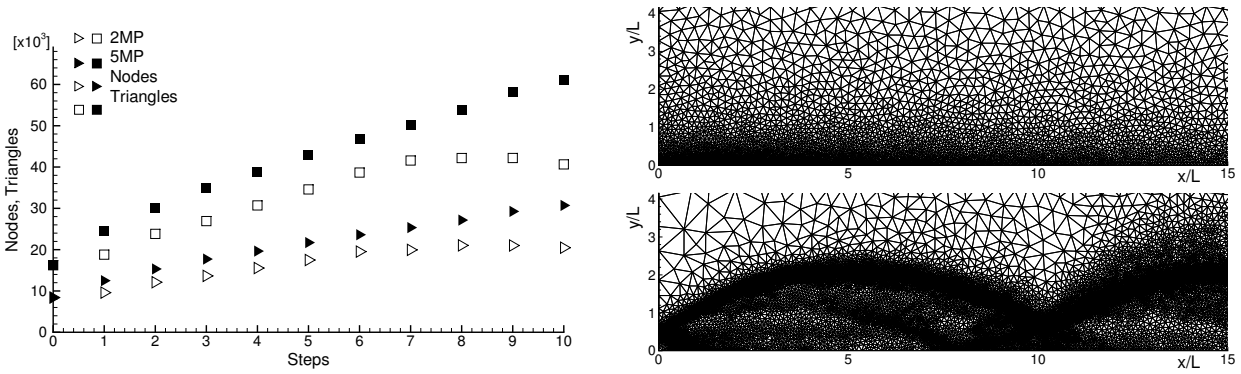

Figure 8: Left: Increase of grid nodes and elements with adaptation steps using 2 and 5 multi-passages and the estimator $\mathcal{H}(P) + \nabla M$ for the nitrogen jet. Right: detail of the initial grid (top) and of the one obtained after 8 adaptation steps (bottom) with the same estimator $\mathcal{H}(P) + \nabla M$ and 5 multi-passages.

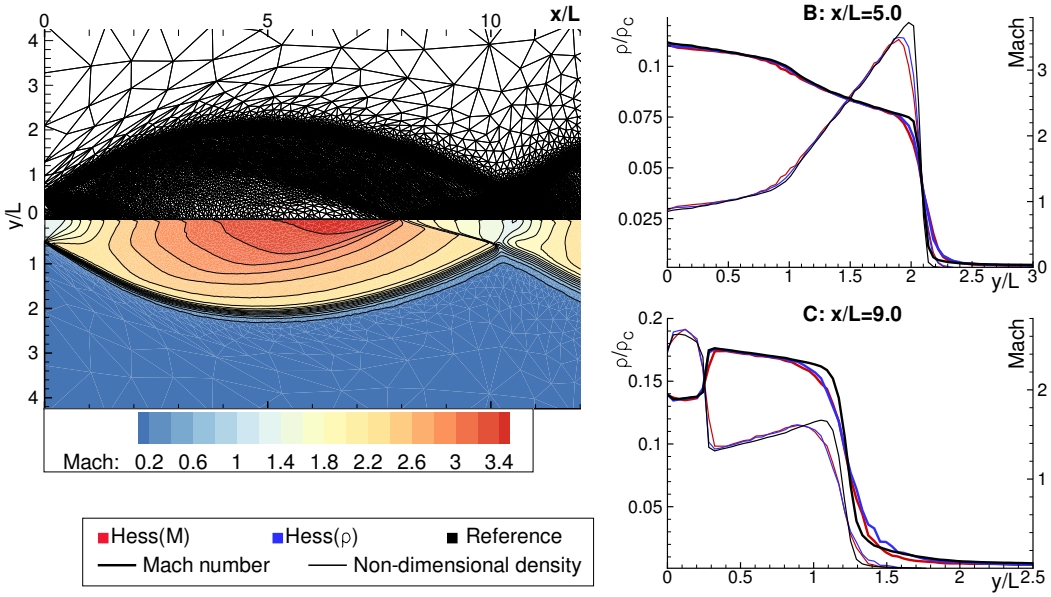

Figure 9: Solutions and grid for the nitrogen jet obtained using the anisotropic estimator based on the complex Hessian of the Mach number and of the density, after five adaptation steps. Reduced density and Mach number are shown at two different positions along the jet center line.

Figure 8 shows the number of grid nodes and elements at each adaptation level for the estimator $\mathcal{H}(P)+\nabla\rho$ using 2 and 5 multi-passages. If only 2 passages are performed, the number of grid nodes reaches a maximum value after seven steps (19 9722 nodes, 41 593 elements). In the following steps, the number of removed nodes is greater then the new ones. When 5 passages are carried out, the number of nodes increases more rapidly during the first five steps, then it follows still an increasing trend but less steep. The same figure shows also a comparison of the initial grid and the one obtained after 8 adaptation steps.

Moreover, also anisotropic estimators are assessed. In this case, single estimators are sufficient to detect all the relevant flow features. Figure 9 displays the solution and the grid after 5 adaptation steps with the anisotropic estimators based on the complex Hessian of the Mach number and the density. Both anisotropic estimators proved to be suitable to efficiently modified the grid. Indeed, with respect to the isotropic cases, less nodes compose the grid at the end of the anisotropic adaptation, namely 23 473 and 21 763 for the $\mathcal{H}^\star(M)$ and $\mathcal{H}^\star(\rho)$, respectively.

Finally, a comparison to the ideal gas model results is performed. The boundary conditions at the nozzle exit section were computed imposing the same ambient conditions, pressure ratios P_e/P_a and P_0/P_e and reservoir pressure of the real-gas case. The numerical values are displayed in the last row of Table 2. Figure 10 compares the solution computed with van der Waals gas model and ideal gas model after eight adaptation steps and using the error estimator $\mathcal{H}(P)+\nabla M$. As expected, the ideal gas model results in different values of Mach number. In particular, the greater Mach number inside the jet leads to a stronger reflected shock, thus a lower Mach downstream. Moreover, a slight difference can be observed also in the location of the shock reflection. Furthermore, the same combination of adaptation parameters applied to the ideal gas case results in a different and less refined grid with respect to the van der Waals model (21 322 nodes).

4.4. Assessment of mesh adaptation criteria in the MDM jet flow

In the previous subsection different adaptation criteria have been assessed for a non-ideal compressible fluid with low molecular complexity. The present section extends the assessment to the sixolane MDM in the thermodynamic region characterized by $0 < \Gamma < 1$, which is a typical effect of the high-molecular complexity. As shown in Figure 4, a jump in density across the slip line is enforced.

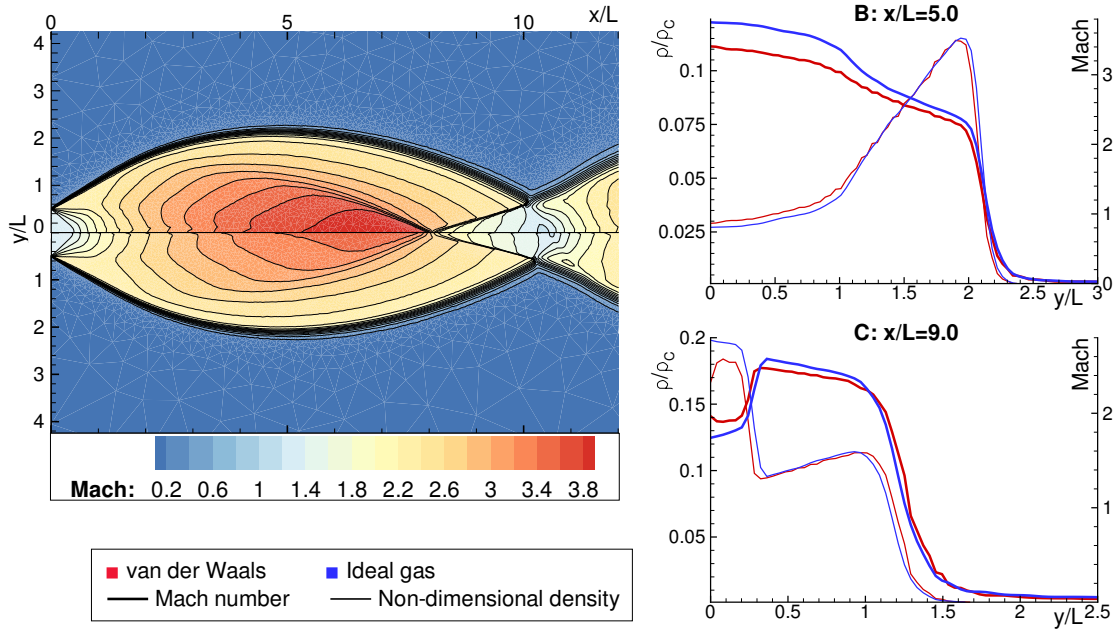

Figure 10: Solutions for the nitrogen jet obtained using the estimator $\mathcal{H}(P) + \nabla M$ and 5 multi-passages with van der Waals gas model (top) and ideal gas model (bottom). Reduced density and Mach number are shown at two different positions along the jet center line.

Following the results obtained for nitrogen gas jets, the compound estimators $\mathcal{H}(P)+\nabla M$ and $\mathcal{H}(P)+\nabla\rho$ are used. Figure 11 shows the results obtained after a different number of adaptation cycles for these isotropic estimators with 5 multi-passage. As in the previous comparisons, the dimensionless density and the Mach number profiles are compared at three different $x = \text{const}$ sections along the jet center-line, but, differently from the nitrogen jet case, the position C (across the reflected shock) is located at $x/L = 11$. In order to detect all the relevant flow structures—in particular the constant-pressure line—with a similar accuracy, a different value of the refinement and coarsening thresholds have been required. For the estimator $\mathcal{H}(P)+\nabla M$ they are equal to $k_R = 2.9$ and $k_C = 0.2$, while for the estimator $\mathcal{H}(P) + \nabla\rho$ they amount to $k_R = 2.6$ and $k_C = 0.22$. In the latter case, the coarsening threshold is modified to avoid and excessive increase of the number of nodes due to a lower refinement threshold. After eight steps a good agreement with the reference solution is obtained for both estimators, as it can be better observed in Figure 12. However, the main difference concerns the number of grid nodes at this step: 13 755 for the estimator containing the gradient of the Mach number and 32 490 for the estimator with the gradient of the density. This discrepancy indicates that the estimator $\mathcal{H}(P) + \nabla M$ is able to modify more efficiently the grid.

Anisotropic error estimators based on flow variables are also assessed. Figure 13 displays the grid and the solution contour plot after 5 anisotropic adaptation steps, using as estimator the complex Hessian of the Mach number, and the density and Mach profiles compared also to the ones obtained with the complex Hessian of the density. As in the isotropic adaptation, the estimator based on the Mach number proved to be more efficient. Indeed, the results obtained with $\mathcal{H}^\star(\rho)$ show a larger deviation from the reference solution, despite a higher number of grid nodes (33 488 compared with 16 252).

An interesting results is shown in Figure 14 which compares the contour plot of the compressibility factor Z on the grid obtained after eight adaptation steps with the isotropic estimator $\mathcal{H}(P) + \nabla M$ and on the initial grid. Thanks to mesh adaptation, a smaller minimum value of the compressibility factor is obtained on the adapted grid, indicating that grid adaptation allows to better capture non-ideal conditions.

Finally, a comparison with the ideal gas model is performed. As suggested by the isentropic expansions in Figure 4, a significant deviation is observed between the solutions obtained with the van der Waals and

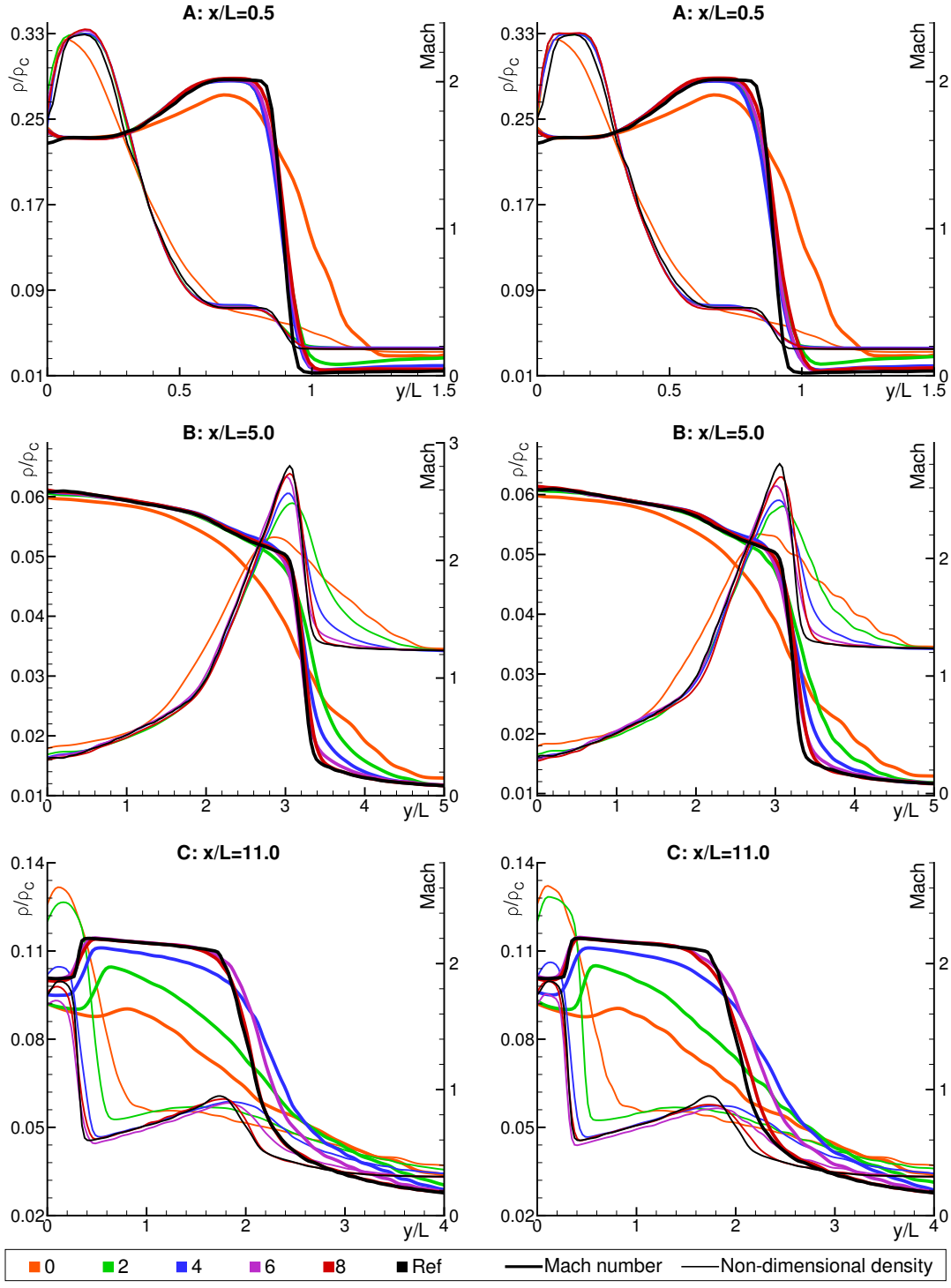

Figure 11: Comparison of the results for the MDM jet obtained with estimators $\mathcal{H}(P) + \nabla M$ (at left) and $\mathcal{H}(P) + \nabla \rho$ (at right) after different adaptation steps (from 0 to 8), using 5 multi-passages. Reduced density and Mach number are shown along three lines at three different positions across the jet center line.

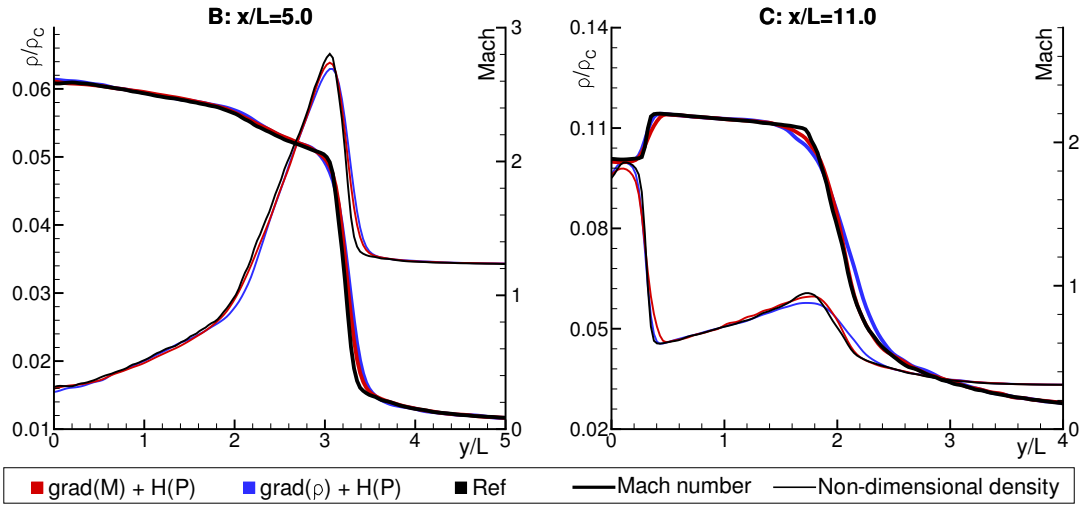

Figure 12: Comparison of the Mach and density profile for the MDM jet obtained with estimators $\mathcal{H}(P)+\nabla M$ and $\mathcal{H}(P)+\nabla\rho$ after eight adaptation steps using 5 multi-passages at two locations.

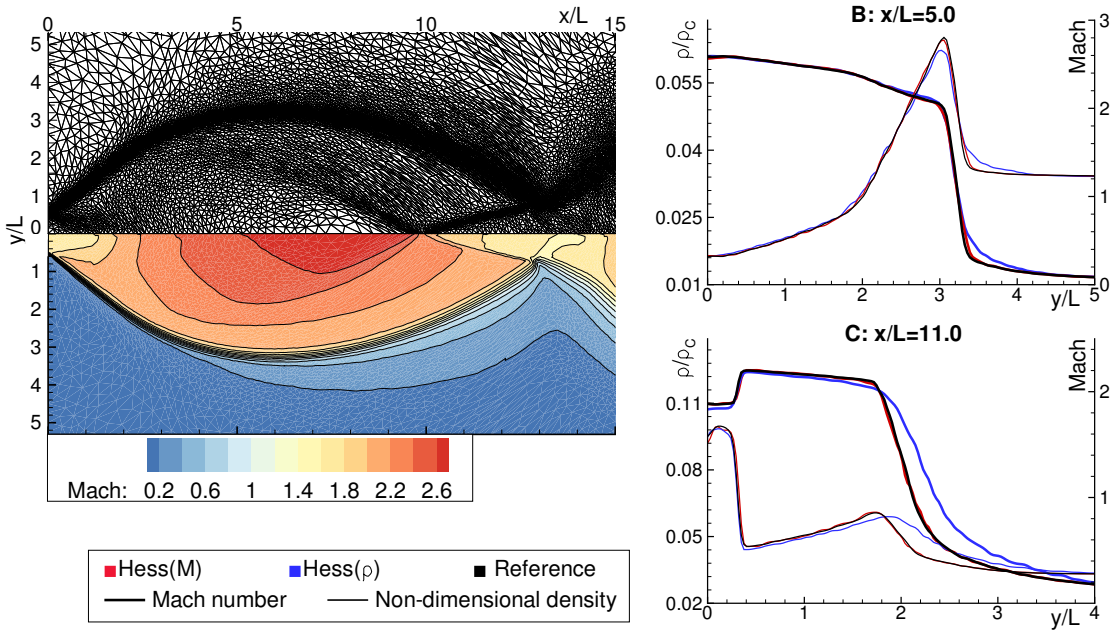

Figure 13: Left: solutions and grid for the MDM jet obtained using the anisotropic estimator based on the complex Hessian of the Mach number, after five adaptation steps. At right, reduced density and Mach number profiled obtained with $\mathcal{H}^\star(M)$ and $\mathcal{H}^\star(\rho)$ are shown at two different positions along the jet center line.

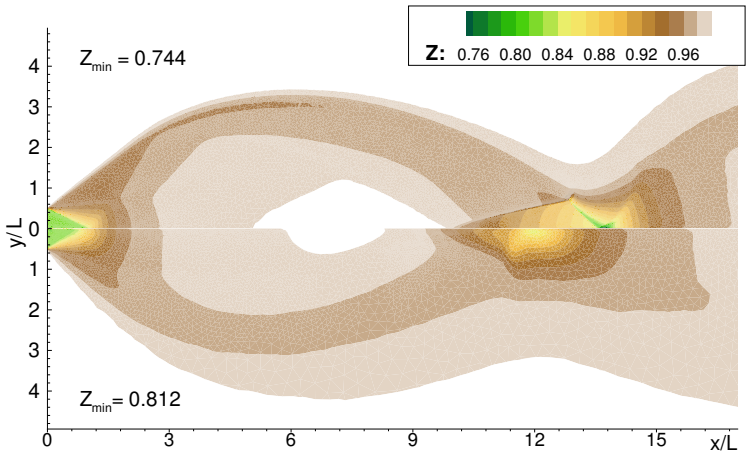

Figure 14: Comparison of the compressibility factor Z for the MDM jet on the adapted grid (top) and on the initial grid (bottom).

the ideal gas model, which are shown in Figure 15. Besides a different position of the reflected shock and different values of Mach number and density, also the size of the jet itself depends on the used thermodynamic model.

5. Discussion and conclusions

Inviscid two-dimensional numerical simulations of under-expanded nozzle jets in the non-ideal compressible-fluid gas region were performed using adaptive unstructured grids. To take into account non-ideal compressible-fluid effects, the van der Waals gas has been chosen to compute the thermodynamic properties of the fluid. Two fluids are simulated: the nitrogen gas, characterized by simple molecules, and the siloxane MDM, which is classified as high-molecular complexity fluid. In both cases, according to the qualitative description of Figure 3, the flow can be defined as weakly under-expanded, since no Mach disk was observed. The capability of the present method to perform mesh adaptation for non-ideal compressible-fluid flows was proved and standard mesh adaptation criteria, widely used under the ideal gas assumption, were compared in this peculiar thermodynamic regime.

Different mesh adaptation criteria and techniques, including multi-passage techniques, edge swapping, grid smoothing, refinement and coarsening, were combined to capture the diverse flow features. The choice of the error estimator was confirmed to be non-trivial for non-ideal compressible-fluid dynamics. For nitrogen jets, isotropic compound estimators combining the Hessian of the pressure and the gradient of the Mach number or density, as well anisotropic estimators based on the complex Hessian of the density and Mach number, proved to be suitable to capture both the reflected shock and the constant-pressure line. No significant differences between Mach- or density-based estimators have been observed. Conversely, for MDM jets, the error estimators based on the Mach number proved to drive more efficiently mesh adaptation, both in isotropic and anisotropic grid adaptation. This difference can be explained by the peculiar non-monotone dependence of the Mach number on the density. According to the quasi mono-dimensional theory, assuming constant specific total enthalpy h^{T} and specific entropy s, the variation of the Mach number with the density can be expressed as [50]

$$\frac{d\,M\big(\rho,s,h^{\mathrm{T}}\big)}{d\rho} = \frac{M\big(\rho,s,h^{\mathrm{T}}\big)}{\rho}\left(1-\Gamma(\rho,s)-\frac{1}{M^2(\rho,s,h^{\mathrm{T}})}\right).$$

Therefore, in the sub-region of the NICFD region where $0 < \Gamma < 1$ the dependence of M on ρ can be non-monotone for supersonic flows. Thus, the Mach number usually presents larger variations with respect

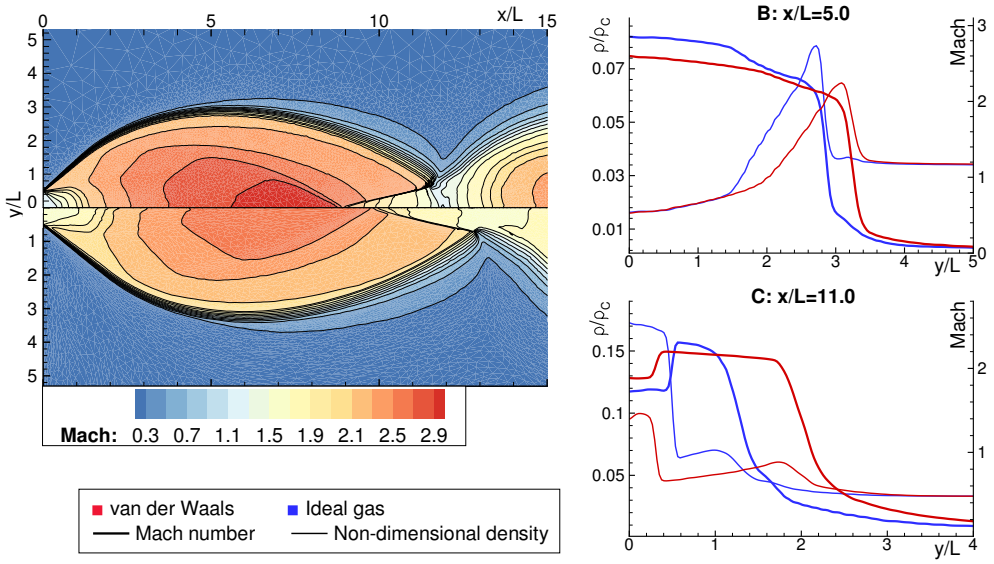

Figure 15: Solutions for the MDM jet obtained using the estimator $\mathcal{H}(P) + \nabla M$ and 5 multi-passages with van der Waals gas model (top) and ideal gas model (bottom). Reduced density and Mach number are shown at two different positions along the jet center line.

to the density, and this feature can be exploited to efficiently perform mesh adaptation in this region, by using error estimators that include the variation of the Mach number.

According to the obtained results, standard mesh adaptation criteria used to build solution-based estimators in ideal gas flows can be successfully applied also in non-ideal compressible fluid region. However, it is the authors' opinion that Mach- and density-based estimators are more suitable for grid adaptation in non-ideal compressible-fluid flows, which are characterized by large fluid compressibility $\kappa = (\partial\rho/\partial P)_s$. As a consequence, for the same expansion ratio, larger density gradients are observed in non-ideal compressible-fluid flows with respect to ideal gas ones. Moreover, Mach number variations are more significant with respect to the ideal gas case because of the dependence of the speed of sound on the density and the temperature that is peculiar of the non-ideal compressible-fluid regime, whereas in ideal gases the speed of sound is a function of the temperature only. Finally, for supersonic flows of high-molecular complexity fluids, if the region of the thermodynamic plane where $0 < \Gamma < 1$ is entered, Mach-based estimators are recommended to exploit the non-monotone M-ρ variation to efficiently perform mesh adaptation. Future developments will concern the assessment of mesh adaptation criteria for unsteady flows in non-ideal compressible-fluid dynamics.

Acknowledgments

Authors want to express their gratitude to Dr. Dario Isola, who provided invaluable suggestions and precious help during the writing of this paper. This research is supported in part by ERC Consolidator Grant N. 617603, Project NSHOCK, funded under the FP7-IDEAS-ERC scheme.

References

[1] J. F. Thompson, B. K. Soni, N. P. Weatherill, Handbook of Grid Generation, CRC Press, 1998.
[2] T. J. Baker, Mesh adaptation strategies for problems in fluid dynamics, Finite Elements in Analysis and Design 25 (3–4) (1997) 243–273, adaptive Meshing, Part 2.
[3] R. Löhner, Mesh Adaptation in fluid Mechanics, Eng. Fract. Mech. 50 (5/6) (1995) 819–847.
[4] D. J. Mavriplis, Unstructured grid techniques, Annual Review of Fluid Mechanics 29 (1) (1997) 473–514.

[5] A. Dervieux, D. Leservoisier, P. L. George, Y. Coudiere, About theoretical and practical impact of mesh adaptation on approximation of functions and solutions of PDE, in: ECCOMAS CFD Conf. Swansea, UK, 2001.
[6] K. Mani, D. J. Mavriplis, Error estimation and adaptation for functional outputs in time-dependent flow problems, J. Comput. Phys. 229 (2010) 415–440.
[7] K. J. Fidkowski, D. L. Darmofal, Output-Based Error Estimation and Mesh Adaptation in Computational Fluid Dynamics: Overview and Recent Results, in: 47th AIAA Aerosp. Sci. Meet. Exhib., 2009.
[8] M. A. Park, Adjoint-Based, Three-Dimensional Error Prediction and Grid Adaptation, AIAA Journal 42 (9) (2004) 1854–1862.
[9] M. Aftosmis, M. Berger, Multilevel Error Estimation and Adaptive h-Refinement for Cartesian Meshes with Embedded Boundaries, AIAA paper 863 (2002) 1–14.
[10] O. Sahni, K. E. Jansen, M. S. Shepard, C. A. Taylor, Adaptive boundary layer meshing for viscous flow simulations, Eng. Comput. 24 (2008) 267–285.
[11] P. J. Frey, F. Alauzet, Anisotropic mesh adaptation for CFD computations, Comp. Meth. Appl. Mech. Engng. 194 (2005) 5068–5082.
[12] F. Dassi, S. Perotto, L. Formaggia, A Priori Anisotropic Mesh Adaptation on Implicitly Defined Surfaces, SIAM Journal on Scientific Computing 37 (6) (2015) A2758–A2782.
[13] J. Peraire, M. Vahdati, K. Morgan, O. Zienkiewicz, Adaptive remeshing for compressible flow computations, J. Comput. Phys. 72 (2) (1987) 449 – 466. doi:http://dx.doi.org/10.1016/0021-9991(87)90093-3.
[14] B. Webster, M. Shepard, Z. Rusak, J. Flaherty, Automated adaptive time-discontinuous finite element method for unsteady compressible airfoil aerodynamics, AIAA journal 32 (4) (1994) 748–757. doi:10.2514/3.12049.
[15] M. Castro-Díaz, F. Hecht, B. Mohammadi, O. Pironneau, Anisotropic unstructured mesh adaption for flow simulations, Int. J. Numer. Meth. Fluids 25 (4) (1997) 475–491.
[16] W. G. Habashi, J. Dompierre, Y. Bourgault, D. Ait-Ali-Yahia, M. Fortin, M.-G. Vallet, Anisotropic mesh adaptation: towards user-independent, mesh-independent and solver-independent CFD. Part I: general principles, Int. J. Numer. Meth. Fluids 32 (2000) 725–744.
[17] Y. Kallinderis, J. Baron, Adaptation methods for a new Navier-Stokes algorithm., AIAA journal 27 (1) (1989) 37–43.
[18] G. P. Warren, W. K. Anderson, S. L. Thomas, James L .and Krist, Grid convergence for adaptive methods, AIAA paper 1592 (1991) 729–741.
[19] S. Choi, J. Alonso, E. van der Weide, Numerical and mesh resolution requirements for accurate sonic boom prediction of complete aircraft configurations., AIAA paper 1060 (2004) 1–33.
[20] K. Hord, Y. Lian, Feature-Based Grid Adaption for the Study of Dynamic Stall, in: AIAA (Ed.), 32nd AIAA Applied Aerodynamics Conference, Vol. 2014–2997, Atlanta (USA), 2014.
[21] A. Kluwick, Theory of shock waves. Rarefaction shocks, in: G. Ben-Dor, O. Igra, T. Elperin, A. Lifshitz (Eds.), Handb. Shock., Vol. 1, Academic Press, 2001, Ch. 3.4, pp. 339–411.
[22] P. A. Thompson, A Fundamental Derivative in Gasdynamics, Physics of Fluids (1958-1988) 14 (9) (1971) 1843–1849.
[23] M. Aftosmis, A second-order TVD method for the solution of the 3D Euler and Navier-Stokes equations on adaptively refined meshes, in: M. Napolitano, F. Sabetta (Eds.), Thirteenth International Conference on Numerical Methods in Fluid Dynamics, Vol. 414 of Lecture Notes in Physics, Springer Berlin Heidelberg, 1993, pp. 235–239.
[24] V. Dolejší, Anisotropic mesh adaptation for finite volume and finite element methods on triangular meshes, Computing and Visualization in Science 1 (3) (1998) 165–178. doi:10.1007/s007910050015.
[25] P. Birkby, G. J. Page, Numerical predictions of turbulent underexpanded sonic jets using a pressure-based methodology, Proceedings of the Institution of Mechanical Engineers, Part G: Journal of Aerospace Engineering 215 (3) (2001) 165–173.
[26] J. Fages, H. Lochard, J.-J. Letourneau, M. Sauceau, E. Rodier, Particle generation for pharmaceutical applications using supercritical fluid technology, Powder Technology 141 (3) (2004) 219–226.
[27] G. Brunner, Supercritical fluids: technology and application to food processing, Journal of Food Engineering 67 (1–2) (2005) 21–33.
[28] P. Colonna, E. Casati, C. Trapp, T. Mathijssen, J. Larjola, T. Turunen-Saaresti, A. Uusitalo, Organic Rankine Cycle Power Systems: From the Concept to Current Technology, Applications, and an Outlook to the Future, Journal of Engineering for Gas Turbines and Power 137 (10) (2015) 100801.
[29] G. Angelino, P. Colonna, Multicomponent Working Fluids For Organic Rankine Cycles (ORCs), Energy 23 (6) (1998) 449–463.
[30] P. Colonna, J. Harinck, S. Rebay, A. Guardone, Real-Gas Effects in Organic Rankine Cycle Turbine Nozzles, Journal of Propulsion and Power 24 (2) (2008) 282–294.
[31] S. Obayashi, Numerical simulation of underexpanded plumes using upwind algorithms, in: AIAA Atmospheric Flight Mechanics Conference, AIAA Paper 88-4360-CP, Minneapolis, United States, 1988.
[32] A. Guardone, M. Parsani, L. Vigevano, Numerical simulations of under-expanded nozzle flows of dense gases, in: XVIII Congress of the Italian Association of Theoretical and Applied Mechanics (AIMETA), Brescia, Italy, 2007.
[33] H. Katanoda, Y. Miyazato, M. Masuda, K. Matsuo, Pitot pressures of correctly-expanded and underexpanded free jets from axisymmetric supersonic nozzles, Shock Waves 10 (2) (2000) 95–101.
[34] H. Katanoda, T. Handa, Y. Miyazato, M. Masuda, K. Matsuo, Effect of Reynolds Number on Pitot-Pressure Distributions in Underexpanded Supersonic Freejets, Journal of Propulsion and Power 17 (4) (2001) 940–942.
[35] A. Guardone, D. Isola, G. Quaranta, Arbitrary Lagrangian Eulerian formulation for two-dimensional flows using dynamic meshes with edge swapping, Journal of Computational Physics 230 (20) (2011) 7706–7722.
[36] D. Isola, A. Guardone, G. Quaranta, Finite-volume solution of two-dimensional compressible flows over dynamic adaptive grids, Journal of Computational Physics 285 (2015) 1–23.

[37] B. Re, An adaptive interpolation-free conservative scheme for the three-dimensional Euler equations on dynamic meshes for aeronautical applications, Ph.D. thesis, Politecnico di Milano (2016).
[38] P. Colonna, T. P. der Stelt, FluidProp: A program for the estimation of thermophysical properties of fluids, Energy Technology Section, Delft University of Technology, The Netherlands (www.fluidprop.com) (2005).
[39] C. Dobrzynski, P. Frey, Anisotropic Delaunay mesh adaptation for unsteady simulations, in: Proceedings of the 17th international Meshing Roundtable, Springer, 2008, pp. 177–194.
[40] R. J. LeVeque, Finite volume methods for conservation laws and hyperbolic systems, Cambridge University Press, 2002.
[41] P. Colonna, A. Guardone, Molecular Interpretation of nonclassical gasdynamics of dense vapors under the van der Waals model, Phys. Fluids 18 (5) (2006) 56101–56114.
[42] H. B. Callen, Thermodynamics and an introduction to thermostatistics, Second Edition, Wiley, 1985.
[43] P. L. Roe, Approximate riemann solvers, parameter vectors and difference schemes, Journal of Computational Physics 43 (2) (1981) 357–372.
[44] B. van Leer, Towards the Ultimate Conservative Difference Scheme, V. A Second Order Sequel to Godunov's Method, Journal of Computational Physics 32 (1) (1979) 101–136.
[45] D. E. Keyes, Aerodynamic applications of Newton-Krylov-Schwarz solvers, in: Fourteenth International Conference on Numerical Methods in Fluid Dynamics, Vol. 453 of Lecture Notes in Physics, Springer Berlin Heidelberg, 1995, pp. 1–20.
[46] R. Löhner, An adaptive finite element scheme for transient problems in CFD, Computer Methods in Applied Mechanics and Engineering 61 (3) (1987) 323–338. doi:http://dx.doi.org/10.1016/0045-7825(87)90098-3.
[47] P. Frey, P.-L. George, Mesh Generation: Application to Finite Element, Vol. 32, Wiley, 2010.
[48] J. Shewchuk, What is a good linear element? Interpolation, conditioning, and quality measures., in: 11*th* International Meshing Roundtable, Ithaca, NY, 2002, pp. 115–126,.
[49] P. A. Thompson, Compressilbe-Fluid Dynamics, McGraw-Hill, 1988.
[50] A. Kluwick, Transonic nozzle flow of dense gases, Journal of Fluid Mechanics 247 (1993) 661–688.